

Deconvolution-based deblurring of reconstructed images in photoacoustic/thermoacoustic tomography

Rejesh, Nadaparambil Aravindakshan; Pullagurla, Harish; Pramanik, Manojit

2013

Rejesh, N. A., Pullagurla, H., & Pramanik, M. (2013). Deconvolution-based deblurring of reconstructed images in photoacoustic/thermoacoustic tomography. *Journal of Optical Society of America A*, 30(10), 1994-2001.

<https://hdl.handle.net/10356/102902>

<https://doi.org/10.1364/JOSAA.30.001994>

© 2013 Optical Society of America. This paper was published in *Journal of Optical Society of America A* and is made available as an electronic reprint (preprint) with permission of Optical Society of America. The paper can be found at the following official DOI: [<http://dx.doi.org/10.1364/JOSAA.30.001994>]. One print or electronic copy may be made for personal use only. Systematic or multiple reproduction, distribution to multiple locations via electronic or other means, duplication of any material in this paper for a fee or for commercial purposes, or modification of the content of the paper is prohibited and is subject to penalties under law.

Downloaded on 20 Mar 2024 20:02:43 SGT

Deconvolution-based deblurring of reconstructed images in photoacoustic/thermoacoustic tomography

Nadaparambil Aravindakshan Rejesh, Harish Pullagurla, and Manojit Pramanik*

Biomedical Imaging Laboratory, Electrical Engineering, Indian Institute of Science, Bangalore 560012, India

*Corresponding author: manojit@ee.iisc.ernet.in

Received July 10, 2013; revised August 19, 2013; accepted August 21, 2013;
posted August 21, 2013 (Doc. ID 193669); published September 12, 2013

Photoacoustic/thermoacoustic tomography is an emerging hybrid imaging modality combining optical/microwave imaging with ultrasound imaging. Here, a *k*-wave MATLAB toolbox was used to simulate various configurations of excitation pulse shape, width, transducer types, and target object sizes to see their effect on the photoacoustic/thermoacoustic signals. A numerical blood vessel phantom was also used to demonstrate the effect of various excitation pulse waveforms and pulse widths on the reconstructed images. Reconstructed images were blurred due to the broadening of the pressure waves by the excitation pulse width as well as by the limited transducer bandwidth. The blurring increases with increase in pulse width. A deconvolution approach is presented here with Tikhonov regularization to correct the photoacoustic/thermoacoustic signals, which resulted in improved reconstructed images by reducing the blurring effect. It is observed that the reconstructed images remain unaffected by change in pulse widths or pulse shapes, as well as by the limited bandwidth of the ultrasound detectors after the use of the deconvolution technique. © 2013 Optical Society of America

OCIS codes: (100.1830) Deconvolution; (170.3010) Image reconstruction techniques; (170.5120)

Photoacoustic imaging.

<http://dx.doi.org/10.1364/JOSAA.30.001994>

1. INTRODUCTION

Photoacoustic/thermoacoustic tomography (PAT/TAT) is an emerging hybrid imaging modality combining optics/microwave imaging with ultrasound imaging [1–7]. PAT/TAT provides structural and functional imaging in diverse application areas, such as breast cancer imaging [7–11], brain imaging [3,12,13], blood vasculature imaging [4,5,14], and sentinel lymph node imaging [15–18], which may have a very significant role in clinical practice in the future starting from diagnosis to the treatment of diseases. In PAT/TAT, nonionizing laser/microwave pulses are delivered into the biological tissues. Some of the delivered energy is absorbed and converted into heat, leading to transient thermoelastic expansion and thus giving wideband ultrasonic emission. The generated ultrasonic waves, known as photoacoustic/thermoacoustic (PA/TA) waves, are then detected by broadband ultrasonic transducers to form images showing the light/microwave absorption map. A single-element ultrasonic transducer or a transducer array is used to obtain the PA/TA waves at various locations around the surface of the tissue. These PA/TA waves are then used to reconstruct the initial pressure rise map. Initial pressure rise is proportional to the absorbed optical/microwave energy. Absorbed energy is proportional to the light/microwave fluence distribution, and the absorption coefficient of the tissue. If a homogeneous fluence distribution is assumed then the initial pressure rise can be used to map the absorption coefficient (optical/microwave) of the tissue.

The factors that affect the PA/TA signals are the optical/microwave absorption properties of tissue, acoustic properties of the tissue, the excitation laser/microwave source characteristics (e.g., pulse width, pulse shape), absorbers' size and

shape, characteristics of the ultrasound sensors (e.g., center frequency, bandwidth, element size and shape), etc. PA/TA signals generated by tumor targets with different sizes subject to microwave pulses with various widths and waveforms were theoretically investigated, and impact of the pulse width on acoustic signal peak-to-peak interval and image spatial resolution was studied [19]. Generated time-domain thermoacoustic pressure is solved analytically and validity of the analytical approach was confirmed by finite-difference time-domain (FDTD) method [20]. Here, a *k*-space pseudo spectral solution is used for the PA/TA wave simulations. In this work, *k*-wave MATLAB Toolbox [21] (MathWorks, Massachusetts, USA) was used for all the PA/TA simulations. The main advantage of the numerical model used in *k*-wave compared to models based on FDTD schemes is that fewer spatial and temporal grid points are needed for accurate simulations leading to faster simulation time and less memory usage.

After analyzing the PA/TA waveforms, numerical phantom was taken and image reconstruction was done to map the initial pressure rise. In practice, instead of delta-pulse, a wider excitation is used. For example, typical thermoacoustic system uses 0.5–1 μ s microwave excitation pulse [7–9,12] and a typical PAT system generally uses 5–10 ns laser pulses [7,10,11]. However, diode lasers, which are increasingly becoming useful for PAT due to their cheaper cost and ultra-compactness, have much longer pulse width (100–200 ns) [22,23] compared to traditional Q-switched pump lasers used in PAT. Thus the PA/TA signal generated gets broadened (due to convolution of system impulse response with the broad excitation pulse) and results in blurring of the reconstructed images. Similar blurring happens due to the limited bandwidth of the ultrasound detectors used in PAT/TAT, as shown theoretically

in the literature [24,25]. For a bandlimited ultrasound transducer, the detected PA/TA signal is the convolution of the PA/TA pressure waves with the transducer impulse response. So, the original PA/TA signal can be restored by deconvolving the transducer impulse response with the detected PA/TA signal. Here, a deconvolution method was used to correct not only for the excitation pulse width but also for the detector bandwidth related blurring through numerical simulations.

Deconvolution in practical situations is considered as an ill-posed problem whose solution cannot be uniquely defined, especially if the data is corrupted with noise [26]. Several algorithms exist to solve the deconvolution problem [27–29]. Here, a least square-based technique was used. Numerical phantoms were used to simulate the blurring effect and then using this algorithm it was demonstrated that it is possible to remove the effect of blurring.

2. METHODS

In this work, a *k*-wave [21] toolbox was used for the simulations of photoacoustics/thermoacoustic signals as well as the reconstruction of the images. The *k*-wave toolbox is a set of open source tool in MATLAB that allows the time domain simulation of PA/TA as well as ultrasound wave propagation and also image reconstruction using time-reversal technique. A desktop with Intel i7 processor and 16 GB RAM was used for all the simulations done in this study.

A. Simulation of PA/TA Waveforms

Figure 1(a) shows the simulation geometry used for the simulation of PA/TA signals for various excitation pulse waveforms and pulse widths. Although the schematic is shown in 2D, the simulations were done in 3D. A computational grid of $210 \times 210 \times 210$ pixels (voxel size 0.025 mm) was used. A perfectly matched boundary layer (PML) was used to satisfy the boundary condition. The detector (red bar) was placed at a distance of 2 mm from the center, where a spherical target of various sizes was placed. Both point detector as well as single element large detector (6 mm diameter nonfocused active area) was used for the simulations. The time step chosen was 10 ns with a total of 728 time steps. The simulations assumed a sound speed of 1570 m/s. For simplicity the medium was considered acoustically homogeneous and there was no absorption or dispersion of sound. However, any other medium (acoustically inhomogeneous) can also be considered. Four types of excitation pulses (sinusoidal, square, Gaussian, and triangular) were used. Figure 1(b) shows various pulse waveforms used for exciting the target (a representative of 2 μ s pulse width is shown). The rise and fall time of the square pulse was chosen to be $t_p/10$, t_p representing the pulse width. Simulations were carried out for various pulse widths (0.25, 0.5, 1, and 2 μ s). The target radius was then varied (0.25, 0.5, 1, and 2 mm) to understand their effect on PA/TA signals. Frequency spectrum of the PA/TA signals was then obtained for further analysis.

B. Deconvolution-Based PA/TA Signal Correction

Another set of simulations was done to show deblurring of reconstructed images using a numerical phantom of blood vessel network. Figure 1(c) shows the blood vessel network and the simulation geometry used for the study. Here, only 2D

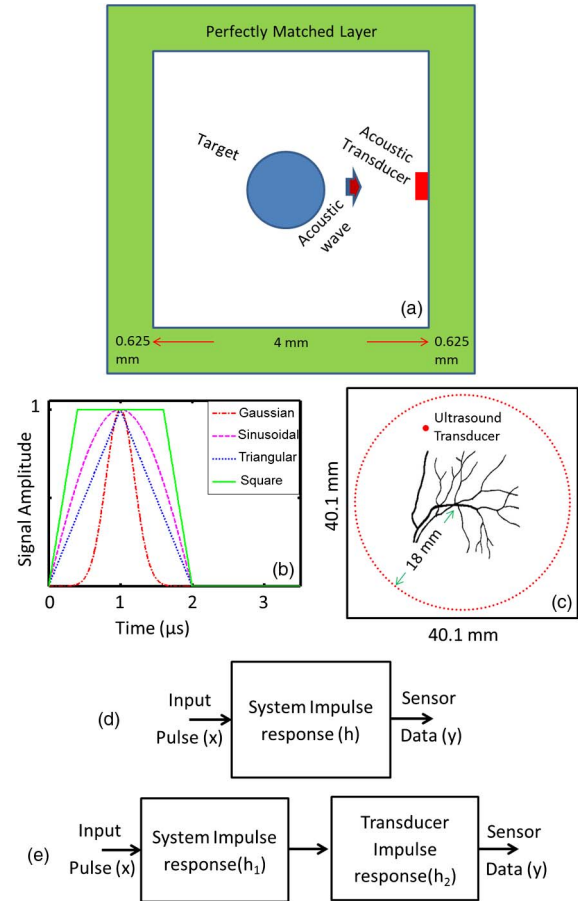


Fig. 1. (a) Schematic diagram of the simulation geometry for PA/TA signal study in 2D. However, actual simulations were done in 3D. (b) The excitation pulse waveforms: sinusoidal, square (rise and fall time of $t_p/10$), Gaussian, and triangular. Pulse width $t_p = 2 \mu$ s. (c) Simulation geometry showing blood vessel network for image reconstruction using deconvolution algorithm. 200 ultrasound transducers were placed at 18 mm distance from the center of the target. (d) A simplified block diagram showing the excitation pulse convoluted with PA/TA system impulse response. (e) Block diagram showing the effect of transducer finite bandwidth in the detected PA/TA signals.

simulations were used (to reduce computational complexity) for generating the PA/TA data and reconstruction of the images. The initial pressure rise in the blood vessels was assumed to be 1 Pa. A computational grid of 401×401 pixels (pixel size 0.1 mm) was used. PML was used here as well. The blood vessel network was placed at the center of the computational grid with 200 ultrasound detectors (red dots) placed on an 18 mm radius circle (spaced equally) to mimic a PAT/TAT setup. Detectors were assumed to be point detector. Sound speed in the medium was assumed to be 1500 m/s. 2500 time steps, each of 10 ns, were used for all computation. 40 dB noise (1% SNR) was added to the PA/TA simulated data. After deconvolution (which will be discussed in the next section) the image reconstruction was done using the time-reversal method in *k*-wave. The signal-to-noise ratio (SNR) was then calculated for the reconstructed images. For calculating SNR, a patch containing 66 pixels on the blood vessel was chosen to form the signal part and a patch containing 441 pixels from the background was chosen to calculate the noise standard deviation. Then SNR is computed as

$$\text{SNR}(dB) = 20 \log(\text{mean signal/noise standard deviation}). \quad (1)$$

C. Deconvolution of PA/TA Signal Using Tikhonov Regularization

Figure 1(d) shows a simplified system diagram to explain the deconvolution process. The forward data, denoted as sensor data vector $y[n]$, is given by

$$y[n] = x[n] * h[n], \quad (2)$$

where $x[n]$ is input signal vector, $h[n]$ is a vector denoting impulse response of the PA/TA imaging system, and $*$ denotes convolution operation. For simplicity the time index n has been omitted now onwards. The impulse response h can be found out by deconvolving y with the input signal x . Deconvolution operation has no direct mathematical definition in time domain. However in frequency domain, the convolution operation becomes multiplication. Applying Fourier transform on Eq. (2) gives

$$Y = XH, \quad (3)$$

where, X , Y , and H represent the Fourier transforms of x , y , and h , respectively. From Eq. (3), H can be written as

$$H = Y/X. \quad (4)$$

h can be obtained by taking inverse Fourier transform of H . But in practice, this direct method is impractical as zeros can be present in the denominator. Also the noise present in the measurement gets amplified largely. In presence of noise Eq. (2) becomes

$$y = x * h + \text{noise}. \quad (5)$$

Because of the presence of noise, a perfect solution is not possible. A least square approximation with Tikhonov regularization [30,31] is proposed here to do the deconvolution. The problem can be rewritten as

$$y = Mh + \text{noise}, \quad (6)$$

where M is the circulant convolution matrix formed from x .

The impulse response using regularization, h_{Tikhonov} , is obtained by minimizing the cost function $A(h)$, given by

$$A(h) = \|y - Mh\|^2 + \lambda \|h\|^2, \quad (7)$$

where λ is the regularization parameter. Equation (7) can be rewritten as

$$A(h) = \{[y - Mh]^T [y - Mh]\} + \lambda (h^T h). \quad (8)$$

The least square minimized solution is obtained by making the gradient of the Eq. (8) to zero, leading to,

$$M^T y = M^T M h_{\text{Tikhonov}} + \lambda h_{\text{Tikhonov}}, \quad (9)$$

where T denotes transpose of a matrix. Equation (9) involves matrices, and matrix inversion is necessary to obtain the

solution. However it can be equivalently written in time domain as

$$x[-n] * y[n] = x[-n] * x[n] * h[n] + \lambda h[n]. \quad (10)$$

In the frequency domain, Eq. (10) transforms to

$$\text{conj}\{X\}Y = [\text{conj}\{X\}]XH_{\text{Tikhonov}} + \lambda H_{\text{Tikhonov}}, \quad (11)$$

where conj represents the complex conjugate operation. From Eq. (11), H_{Tikhonov} can be written as

$$H_{\text{Tikhonov}} = \text{conj}\{X\}Y / [\text{conj}\{X\}X + \lambda]. \quad (12)$$

h_{Tikhonov} can then be obtained by taking the inverse Fourier transform of H_{Tikhonov} . This system impulse response is fed back to k -wave for image reconstruction. Here, λ is tuned to obtain the optimal solution.

D. Effect due to Finite Bandwidth of Transducer

The transducers used for measuring the PA/TA signals are not ideal point detector with infinite bandwidth. The bandwidth of the detectors also has a blurring effect on the reconstructed image. Figure 1(e) shows a simplified system diagram with band-limited transducer in place. The effect of the transducer's bandwidth can also be corrected by assuming the transducer as a filter and deconvolving the transducer response from the sensor data, provided the detectors impulse response is known *a priori*. Generally, the transducer response can be obtained from the manufacturer or can be determined experimentally [28].

Assuming $x * h_2 = z$, it can be written from Fig. 1(e),

$$y = h_1 * z + \text{noise}. \quad (13)$$

By doing mathematical operations similar to those done in the previous section, it can be written:

$$Z^T y = Z^T Z h_1 + \lambda h_1, \quad (14)$$

where, Z is the circulant convolution matrix formed from z . Following the similar procedure mentioned earlier leads to

$$H_{1\text{Tikhonov}} = [\text{conj}(H_2 X)]Y / ([\text{conj}(H_2 X)]H_2 X + \lambda). \quad (15)$$

Taking inverse Fourier transform yields $h_{1\text{Tikhonov}}$, which, is used for image reconstruction, leading to both excitation pulse width and transducer bandwidth correction.

3. RESULTS AND DISCUSSION

A. PA/TA Signals for Varying Pulse Widths with Point Detector

The generated PA/TA pressure waves for impulse, sinusoidal, square, Gaussian, and triangular pulses excitation with various pulse widths (0.25, 0.5, 1, and 2 μs) are shown in Figs. 2(a)–2(e). All signal amplitude was normalized by the maximum pressure amplitude. Here the spherical target radius was fixed at 1 mm. From Fig. 2(b) it is evident that the time duration of the generated PA/TA signals increased with the increase of excitation pulse width, indicating a reduction in the bandwidth of the signal. So for higher pulse width

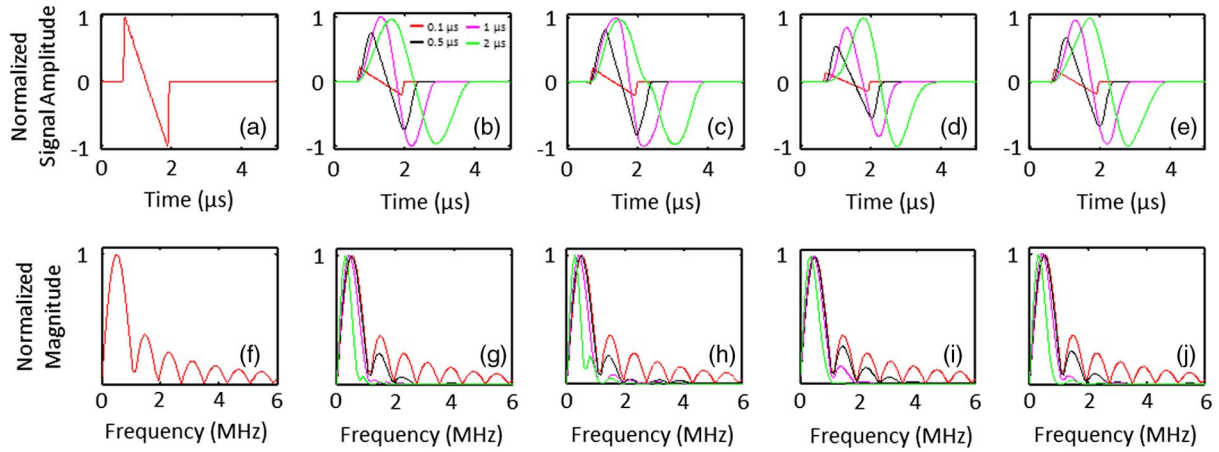


Fig. 2. PA/TA signals generated from 1 mm radius spherical target with (a) impulse, (b) sinusoidal, (c) square, (d) Gaussian, and (e) triangular excitation pulse of varying pulse width. Signals are normalized with maximum signal amplitude. The transducer was assumed to be a point detector. (f)–(j) Spectrum of corresponding PA/TA signals. The spectrum is normalized individually.

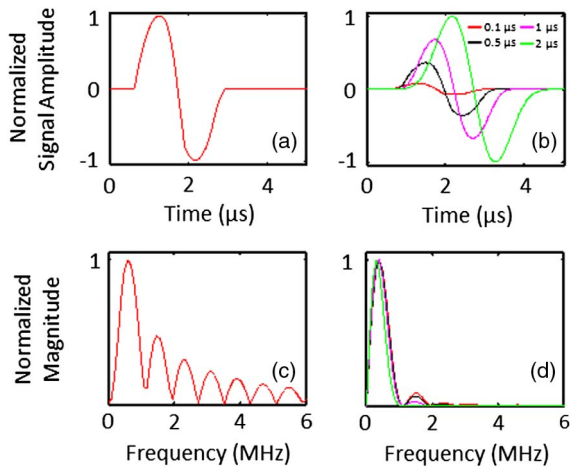


Fig. 3. PA/TA signals detected using broad transducer (6 mm diameter active area transducer), (a) Impulse excitation, (b) Gaussian excitation with various pulse widths. Target object is of 1 mm radius. (c) and (d) Spectrum of corresponding PA/TA signals.

excitation, a low bandwidth transducer can be used for more efficient detection of the signal. Similar results were obtained for other types of excitation pulses, e.g., square, Gaussian, and triangular, as shown in Figs. 2(c)–2(e). When pulse width is

large, the positive and negative lobes in the signal are separated for the square pulse case [Fig. 2(c)], which is obviously distinct from the other three waveforms. When the pulse waveform has a flat part, the time derivative is zero and thus makes no contribution to the initial pressure rise.

The corresponding frequency domain profile (spectrum) for the PA/TA signals is shown in Figs. 2(f)–2(j). The spectral magnitude was normalized (individually) for different pulse widths. A reduction in the side lobes were seen for all excitation pulses as the pulse width increased. The peak frequency of the main lobe decreased as the pulse width increased.

B. PA/TA Signals with Large Detector

The above simulations were repeated for a large nonfocused ultrasound transducer (detector) of 6 mm diameter active area instead of a point detector, as in practice it is difficult to use a point detector in PAT/TAT system due to its low sensitivity. Figure 3(a) shows the PA/TA signal for an impulse excitation with large detector. Figure 3(b) shows similar results [as in the case of point detector, Fig. 2(d)] obtained for a Gaussian pulse excitation for various pulse widths (0.25, 0.5, 1, and 2 μ s), but with large detector. The simulations were done for various excitation pulse waveforms; however, only Gaussian is shown here. Reduction in received signal bandwidth is observed due to the averaging of ultrasound signal over larger

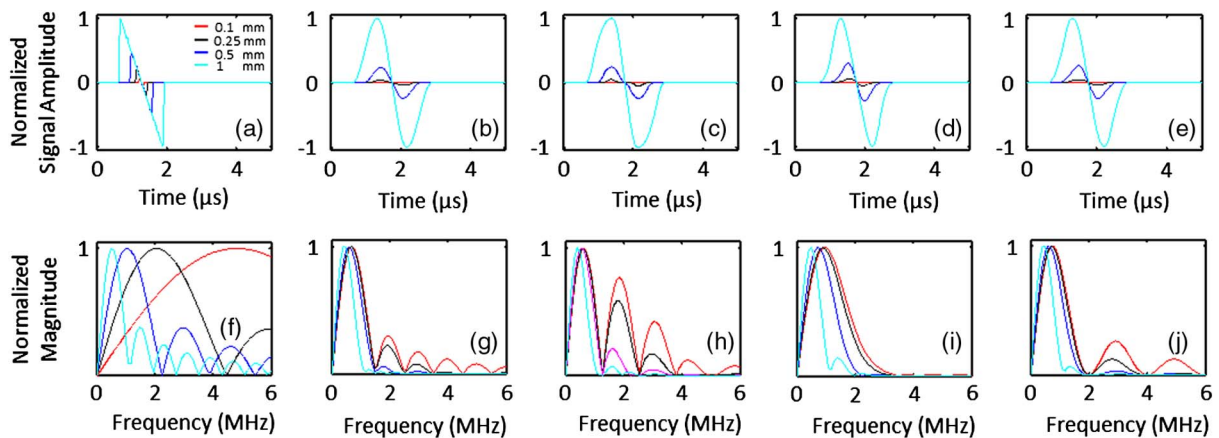


Fig. 4. PA/TA waves generated from various spherical target sizes for (a) impulse, (b) sinusoidal, (c) square, (d) Gaussian, and (e) triangular excitation pulse. Pulse width = 1 μ s. The transducer was assumed to be a point detector. (f)–(j) Spectrum of corresponding PA/TA signals.

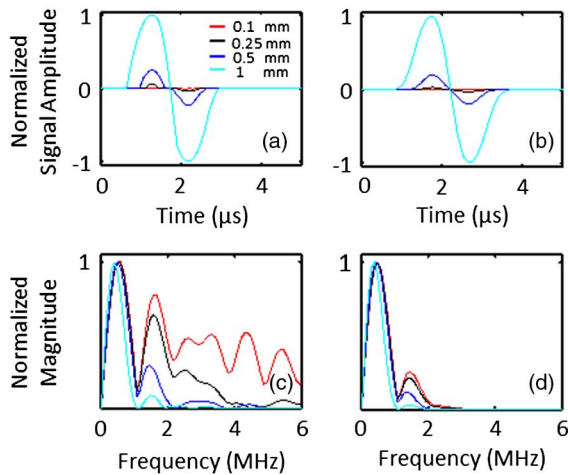


Fig. 5. PA/TA waves generated from varying object size with broad transducer (a) impulse excitation, (b) Gaussian excitation with 1 μ s pulse width. (c) and (d) Spectrum of corresponding PA/TA signals.

active area of the transducer. Note that, when the pulse width is longer, the effect of broad transducer is not noticeable; however, when the pulse width is shorter, the broad active area of the transducer will reduce the effective bandwidth of the detected signal. Figures 3(c) and 3(d) show corresponding frequency spectrum. Note that, the numbers of side lobes were reduced in comparison with the point detector.

C. PA/TA Signals for Varying Target Radius with Point Detector

Figures 4(a)–4(e) show the PA/TA waves for impulse, sinusoidal, square, Gaussian, and triangular excitation pulses (pulse width = 1 μ s) for various target radius (0.1, 0.25, 0.5, and

1 mm). Figures 4(f)–4(j) show the corresponding frequency spectrum. The side lobe reduction was observed for larger targets as well.

D. PA/TA Signals for Varying Target Radius with Large Detector

Figures 5(a) and 5(b) show similar results [similar to Figs. 4(a) and 4(d)] obtained from simulations using various target sizes (0.1, 0.25, 0.5, and 1 mm radius) with broad transducer. The simulations were done for various excitation pulse waveforms. However, results for only Gaussian excitation are shown here. Figures 5(c) and 5(d) show the corresponding frequency spectrum. Note that, the numbers of side lobes were reduced in comparison with the point detector.

E. Removal of Deblurring due to Broad Excitation Using Deconvolution

Next, a numerical blood vessel phantom was used to show the effect of excitation pulse width on the reconstructed image. Figure 6(a) shows the numerical target blood vessel phantom used. The initial pressure rise was assumed 1 Pa. The reconstructed images for a Gaussian pulse excitation with various pulse widths (0.25, 0.5, 1, and 2 μ s) are shown in Figs. 6(b)–6(e). The blurring effect in the reconstructed images was clearly evident and it gets worse with increasing pulse width. Figures 6(f)–6(i) show the corresponding reconstructed images when the PA/TA signals were deconvolved using Tikhonov regularization with $\lambda = 0.1$. As evident from the figures, it was possible to remove the blurring effect of various pulse widths and also to get better quantitative initial pressure rise recovery. Even though the peak values of the reconstructed images varied with different excitation pulses without regularization, peak values of the deconvolved

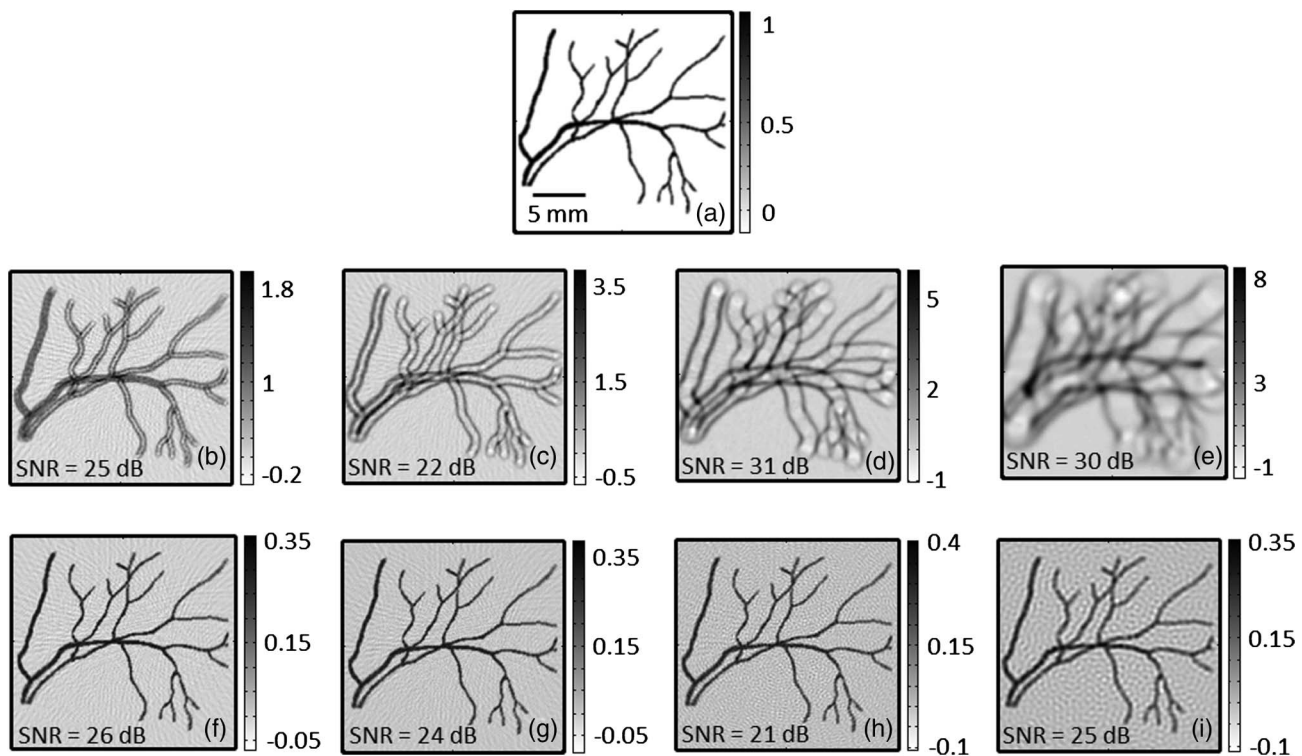


Fig. 6. (a) Numerical blood vessel network phantom. Initial pressure rise assumed to be 1 Pa. Reconstructed images using *k*-wave time reversal method for various excitation pulse widths (b) 0.25 μ s, (c) 0.5 μ s, (d) 1 μ s, and (e) 2 μ s. Excitation pulse is Gaussian. (f)–(i) Corresponding reconstructed images after deconvolution operation.

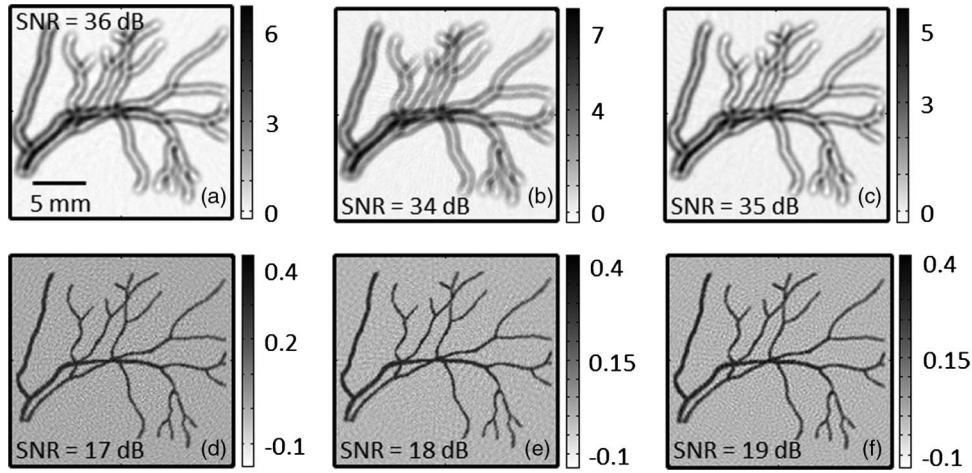


Fig. 7. Reconstructed images for different excitation pulse shape (a) sinusoidal, (b) square, and (c) triangular. Pulse width = $0.5 \mu\text{s}$. (d)–(f) Corresponding reconstructed images after deconvolution operation.

images were found unaffected by change in pulse width or pulse shapes. It is observed that after deconvolution based signal correction was used, the SNR of the reconstructed images reduced with improvement in image resolution and image clarity.

Similar results were obtained with other excitation pulses like sinusoidal, square, and triangular, as shown in Fig. 7. Figures 7(a)–7(c) show reconstructed images without signal correction. The excitation pulse width is fixed at $0.5 \mu\text{s}$. After correcting the signals using deconvolution algorithm (as in the case for Gaussian pulse) reconstructed images were improved significantly as shown in Figs. 7(d)–7(f).

F. Removal of Deblurring due to Broad Excitation and Bandlimited Detectors

In practice, band-limited ultrasonic transducers are used in the PAT/TAT system [7–18]. This once again causes blurring in the reconstructed images. The phantom study shown here demonstrates that the blurring caused by both excitation induced and bandwidth induced can be removed using deconvolution technique as described earlier.

The transducer used in simulations had central frequency of 2.25 MHz and 70% bandwidth. The impulse response of the detector was assumed Gaussian. In practice, *a priori* information about the detector impulse response is required

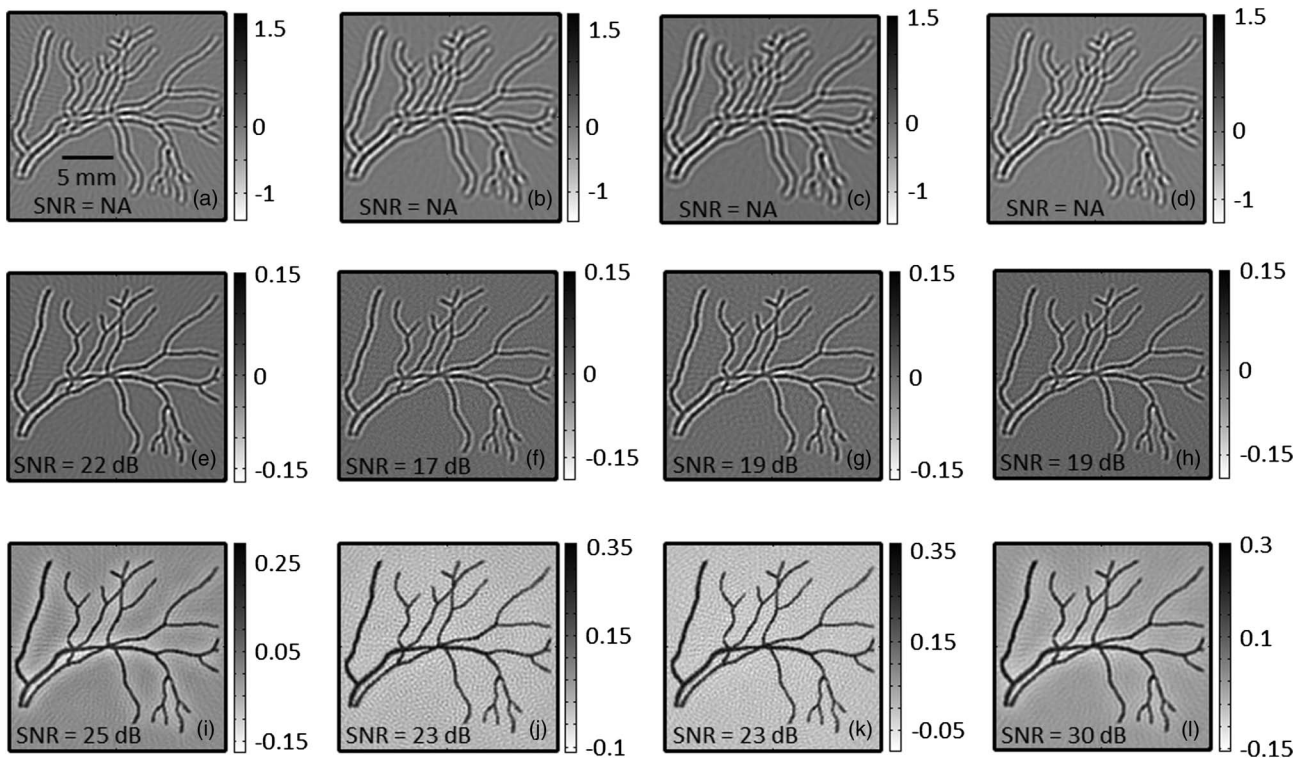


Fig. 8. Reconstructed for different excitation pulse shapes with transducer bandwidth effect (a) Gaussian, (b) sinusoidal, (c) square, and (d) triangular. Pulse width = $0.5 \mu\text{s}$. (e)–(h) Corresponding reconstructed images after deconvolution operation for only excitation pulse width correction. (i)–(l) Corresponding reconstructed images after deconvolution operation for both excitation and transducer bandwidth correction was done.

either from the manufacturer or it needs to be measured experimentally. The reconstructed images for a Gaussian, sinusoidal, square, and triangular pulse excitation of $0.5\ \mu\text{s}$ are shown in Figs. 8(a)–8(d). Figures 8(e)–8(h) show the corresponding images with only signal correction using deconvolution algorithm without taking into consideration the effect of transducer bandwidth [Eq. (12)]. A two-level deconvolution considering the effects due to both excitation pulse width and the transducer bandwidth were performed [Eq. (15)] and the images were shown in Figs. 8(i)–8(l). The images show that both the effect has been significantly removed and the reconstructed images are free of blurring. As before, $\lambda = 0.1$ was used. Since the mean signal value for Figs. 8(a)–8(d) was negative, the SNR values for those figures are marked as “NA.” Note that a two-level deconvolution gives a higher SNR (i)–(l) compared to the corresponding values from one-level deconvolution (e)–(h).

The reconstructed images using the proposed deconvolution method does not show much variation with respect to different types of excitation signals (sinusoidal, Gaussian, etc.) as well as with the variation in pulse widths, which makes the proposed deconvolution method very robust to the shape and duration of the excitation signals. Although we have chosen the regularization parameter manually in this work, methods to compute the optimal regularization parameter automatically have been extensively studied. Recently, an automated way of finding regularization parameter for photoacoustic image reconstruction has been reported [32].

So a two-level deconvolution using the Tikhonov regularization method removes the blurring caused due to finite bandwidth of transducer and due to the excitation pulses. The reconstructed images remain unaffected by change in pulse widths or pulse shapes, as well as by the limited bandwidth of the ultrasound detectors. A more quantitatively accurate initial pressure map is obtained after the deconvolution was done.

4. CONCLUSION

In this work, the effect of different excitation pulse waveforms of different pulse width and different target sizes on the generated PA/TA waves was studied. It was shown that longer pulse width excitation reduces the bandwidth of the generated signals. Also the surface area of the detectors plays a role in the detected signals. Theoretically, one can calculate the generated signals using analytical methods; however, with complicated geometry and inhomogeneous medium, analytical solutions may not exist. Therefore, numerical methods like k -wave-based solution plays an important role in understanding the signal behavior for different imaging configuration in 3D. The problem of deblurring of reconstructed images caused by the broadening of PA/TA signals was addressed by performing a deconvolution using least squares approximate solution with Tikhonov regularization. The images reconstructed from the deconvoluted PA/TA signals were seen to be unaffected by the changing pulse shapes and pulse widths. Moreover, blurring due to the limited bandwidth of the ultrasound detectors was also addressed using the same technique assuming the detectors impulse response is known. At present, the regularization parameter is chosen manually. In the future, an automated way of finding the regularization parameter should be looked into.

ACKNOWLEDGMENTS

The authors would like to thank Bibin Francis, Deepak G. Skariah, and Vijitha Peryasamy for their valuable discussion throughout this work.

REFERENCES

1. L. H. V. Wang and S. Hu, “Photoacoustic tomography: *in vivo* imaging from organelles to organs,” *Science* **335**, 1458–1462 (2012).
2. V. Ntziachristos, J. Ripoll, L. H. V. Wang, and R. Weissleder, “Looking and listening to light: the evolution of whole-body photonic imaging,” *Nat. Biotechnol.* **23**, 313–320 (2005).
3. D. X. Wang, Y. Pang, G. Ku, X. Xie, G. Stoica, and L. H. V. Wang, “Noninvasive laser-induced photoacoustic tomography for structural and functional *in vivo* imaging of the brain,” *Nat. Biotechnol.* **21**, 803–806 (2003).
4. A. A. Oraevsky, “Optoacoustic imaging of blood for visualization and diagnostics of breast cancer,” *Proc. SPIE* **4618**, 81–94 (2002).
5. C. G. A. Hoelen, F. F. M. de Mul, R. Pongers, and A. Dekker, “Three dimensional photoacoustic imaging of blood vessels in tissue,” *Opt. Lett.* **23**, 648–650 (1998).
6. D. Razansky, S. Kellnberger, and V. Ntziachristos, “Near-field radiofrequency thermoacoustic tomography with impulse excitation,” *Med. Phys.* **37**, 4602–4607 (2010).
7. M. Pramanik, G. Ku, C. H. Li, and L. H. V. Wang, “Design and evaluation of a novel breast cancer detection system combining both thermoacoustic (TA) and photoacoustic (PA) tomography,” *Med. Phys.* **35**, 2218–2223 (2008).
8. S. A. Ermilov, T. Khampirad, A. Conjusteau, M. H. Leonard, R. Laceywell, K. Mehta, T. Miller, and A. A. Oraevsky, “Laser optoacoustic imaging system for detection of breast cancer,” *J. Biomed. Opt.* **14**, 024007 (2009).
9. R. A. Kruger, K. D. Miller, H. E. Reynolds, W. L. Kiser, D. R. Reinecke, and G. A. Kruger, “Breast cancer *in vivo*: contrast enhancement with thermoacoustic CT at 434 MHz-feasibility study,” *Radiology* **216**, 279–283 (2000).
10. S. Manohar, S. E. Vaartjes, J. C. G. van Hespén, J. M. Klaase, F. M. van den Engh, W. Steenbergen, and T. G. van Leeuwen, “Initial results of *in vivo* non-invasive cancer imaging in the human breast using near-infrared photoacoustics,” *Opt. Express* **15**, 12277 (2007).
11. D. Piras, W. Steenbergen, T. G. van Leeuwen, and S. Manohar, “Photoacoustic imaging of the breast using the twente photoacoustic mammoscope: present status and future perspectives,” *IEEE J. Sel. Top. Quantum Electron.* **16**, 730–739 (2010).
12. Y. Xu and L. H. V. Wang, “Rhesus monkey brain imaging through intact skull with thermoacoustic tomography,” *IEEE Trans. Ultrason. Ferroelectr. Freq. Control* **53**, 542–548 (2006).
13. C. H. Li and L. H. V. Wang, “Photoacoustic tomography of the mouse cerebral cortex with a high-numerical-aperture-based virtual point detector,” *J. Biomed. Opt.* **14**, 024047 (2009).
14. R. I. Siphanto, K. K. Thumma, R. G. M. Kolkman, T. G. van Leeuwen, F. F. M. de Mul, J. W. van Neck, L. N. A. van Adrichem, and W. Steenbergen, “Serial noninvasive photoacoustic imaging of neovascularization in tumor angiogenesis,” *Opt. Express* **13**, 89–95 (2005).
15. K. H. Song, E. W. Stein, J. A. Margenthaler, and L. H. V. Wang, “Noninvasive photoacoustic identification of sentinel lymph nodes containing methylene blue *in vivo* in a rat model,” *J. Biomed. Opt.* **13**, 054033 (2008).
16. T. N. Erpelding, C. Kim, M. Pramanik, L. Jankovic, K. Maslov, Z. Guo, J. A. Margenthaler, M. D. Pashley, and L. H. V. Wang, “Sentinel lymph nodes in the rat: noninvasive photoacoustic and U.S. imaging with a clinical U.S. system,” *Radiology* **256**, 102–110 (2010).
17. D. Pan, M. Pramanik, A. Senpan, S. Ghosh, S. A. Wickline, L. H. V. Wang, and G. M. Lanza, “Near infrared photoacoustic detection of sentinel lymph nodes with gold nanobeacons,” *Biomaterials* **31**, 4088–4093 (2010).

18. M. Pramanik, K. H. Song, M. Swierczewska, D. Green, B. Sitharaman, and L. H. V. Wang, "In vivo carbon nanotube-enhanced non-invasive photoacoustic mapping of the sentinel lymph node," *Phys. Med. Biol.* **54**, 3291–3301 (2009).
19. X. Wang, D. R. Bauer, J. L. Vollin, D. G. Manzi, R. S. Wittie, and H. Xin, "Impact of microwave pulses on thermoacoustic imaging applications," *IEEE Antennas Wireless Propag. Lett.* **11**, 1634 (2012).
20. C. Lou, L. Nie, and D. Xu, "Effect of excitation pulse on thermoacoustic signal characteristics and the corresponding algorithm for optimization of image resolution," *J. Appl. Phys.* **110**, 083101 (2011).
21. B. E. Treeby and B. T. Cox, "k-wave: MATLAB toolbox for the simulation and reconstruction of photoacoustic wave-fields," *J. Biomed. Opt.* **15**, 021314 (2010).
22. R. G. M. Kolkman, W. Steenbergen, and T. G. V. Leeuwen, "In vivo photoacoustic imaging of blood vessels with a pulsed laser diode," *Lasers Med. Sci.* **21**, 134–139 (2006).
23. L. Zeng, G. Liu, D. Yang, and X. Ji, "3D-visual laser-diode-based photoacoustic imaging," *Opt. Express* **20**, 1237–1246 (2012).
24. M. Haltmeier and G. Zangerl, "Spatial resolution in photoacoustic tomography: effects of detector size and detector bandwidth," *Inverse Probl.* **26**, 125002 (2010).
25. M. Xu and L. H. V. Wang, "Analytic explanation of spatial resolution related to bandwidth and detector aperture size in thermoacoustic or photoacoustic reconstruction," *Phys. Rev. E* **67**, 056605 (2003).
26. S. M. Riad, "The deconvolution problem: an overview," *Proc. IEEE* **74**, 82–85 (1986).
27. Y. Wang, D. Xing, Y. G. Zeng, and Q. Chen, "Photoacoustic imaging with deconvolution algorithm," *Phys. Med. Biol.* **49**, 3117–3124 (2004).
28. T. Lu and H. Mao, "Deconvolution algorithm with LTI Wiener filter in photoacoustic tomography," in *Photonics and Optoelectronics SOPO*, Wuhan, 2009.
29. Z. Dogan, T. Blu, and D. van de Ville, "Eigensensing and deconvolution for the reconstruction of heat absorption profiles from photoacoustic tomography data," in *Proceedings of the Tenth IEEE International Symposium on Biomedical Imaging: From Nano to Macro (ISBI'13)* (IEEE, 2013), pp. 1142–1145.
30. A. N. Tikhonov and V. Y. Arsenin, *Solution of Ill-Posed Problems* (Halsted, 1977).
31. R. C. Aster, B. Borchers, and C. H. Thurber, *Parameter Estimation and Inverse Problems* (Elsevier, 2013).
32. C. B. Shaw, J. Prakash, M. Pramanik, and P. K. Yalavarthy, "LSQR-based decomposition provides an efficient way of computing optimal regularization parameter in photoacoustic tomography," *J. Biomed. Opt.* **18**, 080501 (2013).